Author's Accepted Manuscript

Imaging of Fast Neutrons and Gamma Rays from ^{252}Cf in a Heavily Shielded Environment

Jonathan S. Beaumont, B. Alan Shippen, Matthew P. Mellor, Malcolm J. Joyce

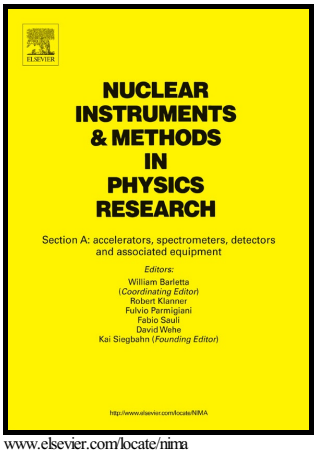

www.elsevier.com/locate/nima

PII: S0168-9002(16)31196-2
DOI: http://dx.doi.org/10.1016/j.nima.2016.11.043
Reference: NIMA59462

To appear in: *Nuclear Inst. and Methods in Physics Research, A*

Received date: 19 June 2016
Revised date: 16 November 2016
Accepted date: 21 November 2016

Cite this article as: Jonathan S. Beaumont, B. Alan Shippen, Matthew P. Mello and Malcolm J. Joyce, Imaging of Fast Neutrons and Gamma Rays from ^{252}Cf i a Heavily Shielded Environment, *Nuclear Inst. and Methods in Physic Research, A,* http://dx.doi.org/10.1016/j.nima.2016.11.043

This is a PDF file of an unedited manuscript that has been accepted fo publication. As a service to our customers we are providing this early version o the manuscript. The manuscript will undergo copyediting, typesetting, an review of the resulting galley proof before it is published in its final citable form Please note that during the production process errors may be discovered whic could affect the content, and all legal disclaimers that apply to the journal pertain

ACCEPTED MANUSCRIPT

Imaging of Fast Neutrons and Gamma Rays from ^{252}Cf in a Heavily Shielded Environment

Jonathan S. Beaumont[a,*], B. Alan Shippen[b], Matthew P. Mellor[b], Malcolm J. Joyce[a]

[a]*Department of Engineering, Lancaster University, Lancashire, LA1 4YW, UK*
[b]*Createc Ltd. Derwent Mills Commercial Park, Cockermouth, Cumbria, CA13 0HT, UK*

Abstract

A 75 MBq ^{252}Cf neutron source stored inside a steel water tank was characterised using a compact fast-neutron and gamma-ray imaging system based on a passive slot modulation imaging technique. Radiation fields were imaged from a variety of positions with the source in the stored position (located in the center of the water tank: high shielding) and in the exposed position (located at the edge of the water tank: low shielding). It was possible to locate the ^{252}Cf source in each image and gain additional information of the neutron and gamma-ray fields in the local environment including scatter contributions from the steel shield, floor and walls in proximity to the source. A long exposure image of the stored source, taken over thirty days, identified the location of the radiation source from the low dose (<1μSv/h) field penetrating through 46 cm of water in the storage tank.

Keywords:
Neutron imaging
Gamma ray imaging
MCNP5

1. Introduction

Passive radiation imaging is the use of a radiation "camera" to quantify the origin of radiations in a local environment i.e. to visually assay radiation sources in proximity to the imager. Passive imagers do not require a radiation source, relying on the fields produced by the materials under investigation. Imaging the neutron and gamma-ray fields provides an additional sensitivity to materials which emit both radiation types. Mixed-fields are less likely to be masked from search due to the fundamental differences in material interactions; for example high-Z materials will shield gamma-rays but do not shield neutrons effectively [1]. Pulse shape discrimination is now a viable method for discriminating neutrons and gamma rays in solids and high-flashpoint liquids [2] [3] increasing the range of options available for these types of deployments.

A major advantage of imaging the fast-neutron field is that such fields are often produced by nuclear materials and therefore could be used to identify and locate agglomerations of plutonium or other transuranics; such as in nuclear fuels, or in process streams. These capabilities make such a system attractive for nuclear decommissioning, to locate materials which require attention. Knowledge of the location allows the subsequent required actions to be planned strategically. There is also the possibility to investigate the emission of neutrons from accelerators, or critical reaction chains such as fission and fusion reactors. Fast-neutron fields are highly penetrating and can pass through significant quantities of lead and hydrogenous shielding materials. Imaging systems have been used to date to image neutron sources through hydrogenous shielding [4] [5]. The ability to discern fuel debris from other radiation sources has been highlighted in a recent report on the decommissioning of the Fukushima Daiichi reactors [6]. Current methods of fuel debris assay include muon tomography, a method which has been used recently at Fukushima Daiichi [7], though, unlike a neutron imaging approach, there is no information about any stimulated fission reactions occurring within the core containment. Fast-neutron imaging has been used in high-dose fields to characterise the fission reaction within a nuclear reactor [8], making steps towards using this technology for re-

*Corresponding author
Email address: j.beaumont@lancaster.ac.uk (Jonathan S. Beaumont)

Accepted manuscript

ACCEPTED MANUSCRIPT

actor decommissioning. The ability to confirm localised absence of neutron emitting materials is also practical for decommissioning purposes and may be applicable to some nuclear safeguards applications.

There are many situations where neutron and gamma-ray fields are complex and not calculable if the layout of radiation source terms in not known. Precise physical characterisation of these fields through measurement can be used to complement simulated results from radiation transport codes. Physical measurements can be beneficial at addressing shortcomings in modelling capability caused by inconsistencies between real and modelled systems. Such functions may apply to reactors for research purposes, or to accelerators used in medical procedures where secondary patient dose must be kept to a minimum. These types of measurements can also be used to determine the unknown abundance and layout of materials in a given environment. For example fast-neutron imaging has recently been used by the lunar prospector to investigate the presence of water near the lunar surface [9]. Neutron fields can be characterised with other portable systems such as neutron scatter cameras [10] [11] though these systems involve multiple detectors and lack compactness and radiation hardness.

2. Materials

2.1. Radiation Environment

This paper describes the imaging of a 75 MBq ^{252}Cf source contained within a 93 × 93 × 90 cm light water tank and surrounded by 3.3 cm of steel on all sides. The source is located by default centrally in the horizontal X-Y plane in the water tank, 35 cm above the concrete floor. In this position the source is referred to as "stored" where it is heavily shielded (neutron dose <1μSv/h at tank edge on all sides). A pneumatic system is used to move the source horizontally to the tank edge allowing a large number of neutrons, of the order 10^7 neutrons s^{-1}, to escape the tank; this configuration is referred to as "exposed". The surrounding civil structure of concrete and concrete block shields radiation to the outside world. The imaging measurements described in this work were conducted as a survey from quasi-randomly selected locations within a field of view of the source location. A survey point in close proximity of the tank edge was chosen for the shielded source image to optimise the amount of data collected associated with the weak field permeating through the water (46 cm) and steel (3.3 cm) shields.

2.2. Radiation Imaging System

The imaging survey was conducted with a prototype fast-neutron imaging system based upon the principle of a single collimated detector [12] [13]. This system is compact and portable, weighing 20 kg. The imaging probe retains a small form factor within 20 × 20 × 35 cm and therefore can be deployed in restrictive spaces and at multiple locations allowing surveys to be easily implemented. The system relies on neutrons having few scatters in the major medium of the local environment i.e. air such that the angle of incidence on the probe relates back to the origin of the neutron emission (or scatter within a material such as water).

The system comprises a front-end probe containing a single collimated detector and mechatronics; data acquisition and a PC. The detector is shielded with tungsten and high-density polyethylene (HDPE) to create a biased spatial sensitivity of the detector to neutron and gamma-ray radiation in the surrounding space [14]. The collimator geometry is cylindrical with a 6 mm slot void cut into the face of the tungsten and HDPE. The resulting sensitivity matrix is mostly low (high shielded) with a roughly rectangular unshielded 'field of view' region of high relative sensitivity. The neutron sensitivity matrix can be seen in Fig. 1(a) the gamma-ray sensitivity matrix in Fig. 1(b). Motors within the probe rotate the collimator, and consequently the spatial sensitivity map, through two perpendicular axes (vertical through the probe body: pan angle; and horizontal through the cylindrical axis of the collimator: slot angle). This allows the radiation field emitted from the surrounding space to be evaluated in correspondence with each element of the sensitivity matrix. During the scanning procedure the slot and pan angles and varied systematically over the predefined range whilst data are accumulated for a constant time t_d at each collimator position. A single 6 ml EJ-301 [15] liquid scintillation detector (Scionix, Netherlands), sensitive to both gamma rays and neutrons, is used to detect radiation within the collimator. Radiation events at the detector are processed using a mixed-field analyser (Hybrid Instruments, UK) [16] [17] which discriminates neutrons and gamma rays in real-time using a pulse-gradient analysis algorithm on an on-board FPGA [18]. The number of neutrons and gamma-rays detected during time t_d at each collimator position are counted using an array of 32-bit binary counters which are interfaced with the PC through a micro-controller. A secondary 10 × 10 × 10 cm EJ-309 liquid scintillation detector (Scionix, Netherlands) of similar response [19] was incorporated into the imaging system using the same discrimination and data acquisition modules to measure the neutron and gamma-

Accepted manuscript

ACCEPTED MANUSCRIPT

ray backgrounds during the imaging routine in synchronisation with each collimator position.

The acquired data D are related to the sensitivity matrix M and the image I by Eq. (1). M is calculated from detailed models of the imaging probe using the Monte Carlo radiation transport code MCNP5 and are seen in Fig. 1. The image I can be calculated from M and D using an algebraic reconstruction technique (ART) [20], a single iteration of which is outlined in Eq. (2). Here d_j is the j^{th} row of D, m_j is the j^{th} row of M and λ_k is a relaxation parameter. Images are solved to convergence with $1^\circ \times 1^\circ$ pixel resolution.

$$D = MI \tag{1}$$

$$I^{k+1} = I^k + \lambda_k \frac{d_j - \langle m_j, I^k \rangle}{\|m_j^2\|} m_j \tag{2}$$

If the situation permits, it is possible to produce a wide angle optical image stitched from multiple shots from a digital camera from the same image origin and the same coordinate system as the output radiation image. The radiation images can then be overlaid onto the optical images to visualise the radiation distribution with relation to optically visible objects.

3. Experimental Method

A scale diagram of the radiation laboratory at Lancaster University, UK in which the measurements were made is shown in Fig. 2 showing the ^{252}Cf source, water tank, steel shielding and surrounding structure. The three survey points A-C are shown on this diagram in the X-Y plane. The ^{252}Cf source was located 35 cm from the floor and could be located in two positions: in the center of the tank in the X-Y plane (the stored position), or at the edge of the water tank (the exposed position). A summary of the survey points is given in Table 1 including the height of the image origin above the concrete floor and r_{SI} the direct distance from the source to the image origin.

At each survey point the probe was placed such that the location was derived from the position of the detector i.e. the image origin. Photographs of the imaging system performing surveys B and C can be seen in Fig. 3 and Fig. 4 respectively. The desired image routine parameters were entered into the data acquisition system, the source was then exposed if required and the imaging routine was started. The imaging system was then left to complete the routine acquiring the number of neutron and gamma-ray detections at each collimator position for time t_d. The neutron and gamma-ray

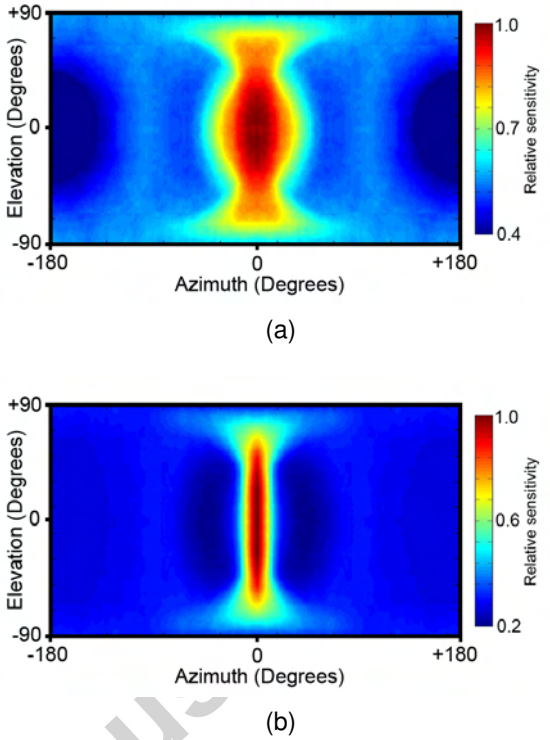

Figure 1: Sensitivity maps of collimated detector to (a) ^{252}Cf neutrons and (b) ^{252}Cf gamma rays in all space surrounding the detector. The sensitivity maps shown here comprise a single element of the sensitivity matrix M.

Table 1: Parameters associated with imaging survey of ^{252}Cf tank

Survey pt	r_{SI}^a	Source	Dose	t_d (s)
A	237 cm	Exposed	3 μSv/h	35
B	157 cm	Exposed	15 μSv/h	20
C	94 cm	Stored	<1 μSv/h	300

[a] Distance from the source to the image origin

background rates using the same electronic processing were also monitored as a quality check in synchronisation with the image data collection to help account for any temperature associated gain drift and other effects. The total data acquisition times for images at survey points A, B and C were 40 hours, 72 hours and 30 days respectively. Once the data acquisition phase was completed, the neutron and gamma-ray images at each survey point were solved using the ART algorithm described in section 2.2 and was overlaid on an optical image where appropriate (survey point C located too close for an interpretable optical image).

Accepted manuscript

ACCEPTED MANUSCRIPT

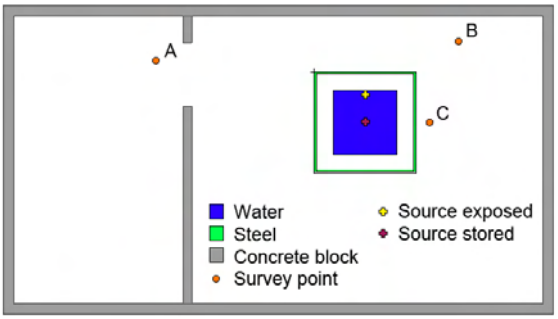

Figure 2: Layout of the lab environment and model for Monte Carlo interrogation in X-Y plane i.e. overhead view. The ^{252}Cf source is contained within a cubic meter of water, and surrounded by 3.3 cm of steel shielding. The room has concrete block walls and a concrete floor. Images were taken from points A, B and C with the source exposed (moved to the outside edge of the water tank) or stored (in the center of the water tank) as appropriate.

Figure 3: The imaging system collecting image data at survey point B with the source exposed. This corresponds to the radiation images displayed in Figs. 6(b) and 7(b).

Figure 4: The imaging system collecting image data at survey point C with the source stored. This corresponds to the radiation images displayed in Figs. 10(a) and (b).

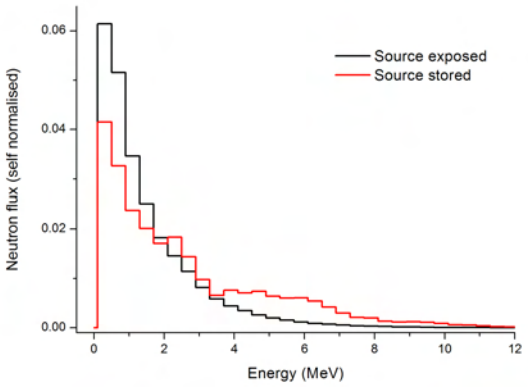

Figure 5: Simulated neutron flux versus energy at position B with source exposed in contrast to the neutron flux at position C with the source stored. These simulations were performed in MCNP5 using the model shown in Fig. 2 and at the appropriate heights given in Table 1.

4. Monte Carlo Method

The Monte Carlo code MCNP5 [21] was used in this work to calculate the neutron and gamma-ray system matrices, simulate pin-hole images, and to calculate flux and energy spectra.

4.1. System Matrices

The imaging probe was modelled in MCNP5 and was interrogated using a plane source of mono-directional radiation simulating a point source from infinity. This source was rotated through 4π at a fixed distance with single degree steps in azimuth and elevation, the flux was tallied at the detector at each of these points and was used to create a full-universe sensitivity map of the collimated detector to neutrons and gamma-rays corresponding to a single orientation of the collimator. A geometric transformation was then applied to this single element to unfold the remainder of the sensitivity matrix for neutrons and gamma-rays. Single elements of the neutron and gamma-ray sensitivity matrices are shown in Fig. 1.

4.2. Flux Simulations

The model for MCNP5 interrogation is summarised in Fig. 2. In addition to the structures shown a concrete floor was also included. A void sphere was modelled at each survey point, and the source location was set to the appropriate stored or exposed position. The neutron flux distribution was tallied at each survey point, a comparison of which can be seen in Fig. 5.

ACCEPTED MANUSCRIPT

4.3. Pin-hole Image Simulations

The pin-hole flux tally in MCNP5 was used to form simulated images of the ^{252}Cf tank for comparison with the experimentally obtained images. The environment was modelled to detail as in section 4.2. The radiation imager was modelled as a perfect pin-hole camera with $1^\circ \times 1^\circ$ pixels in azimuth-elevation to match the resolution output from experimental images. The imager was then incorporated into the model at survey points A, B and C with the center of the image aligned with the source location i.e. 'looking' directly at the source. The flux was calculated using 100 keV bins, and was modified with a detector efficiency function and point-spread function to produce an image comparable to that seen by the physical imaging system.

5. Results

5.1. Exposed Source Imaging

The source was configured in the exposed position, the probe was placed sequentially at two locations in the corners of the room representing possible deployment positions at different distances from the source and at different heights. The field of view was set to include the tank as a source of radiation. The neutron and gamma-ray background rates monitored by the larger EJ-309 detector as described and were not seen to drift or change during the imaging routine. The results of the neutron and gamma-ray imaging of the exposed source are shown in Figs. 6 and 7 respectively. These images show the measured distribution of radiation incident on the probe projected onto optical images of the surrounding environment; allowing the imaged radiation fields to be associated with objects in the environment. These images each show a single radiation hotspot inside the storage tank and are not radially symmetric as might be expected from the image of a point source. The images show some skewing and additional features which may represent radiation incident on the probe from regions other than the ^{252}Cf source location in the neutron and gamma-ray fields.

MCNP5 simulations accompanying these radiation images are shown in Figs. 8 and 9. Simulated images were produced with the MCNP5 pin-hole camera feature from the same locations as the experimental images were taken, and are therefore useful as direct comparisons with the experimentally obtained images. The images were simulated using a perfect pin-hole function, a Gaussian blur function was then applied (a 2D gaussian smoothing kernel with a range of 20×20 pixels and standard deviation of 2.3) to more closely simulate the non-zero point spread function of the physical imaging system. The filter parameters were chosen by comparing experimentally obtained point-source images and MCNP5 pin-hole camera images. Filters applied to the Monte Carlo image were assessed qualitatively to determine the parameters which performed the most realistic transformation when compared with real image solutions. These simulated images are centred upon the location of the ^{252}Cf source.

The simulations shown in Figs. 8(a) and (b) correspond to the neutron images produced from survey points A and B respectively. These simulated images show a central hotspot, with other smaller contributions from other areas close to the central location. The plots shown in Fig. 8(c) shows the interactions of neutrons in the environment in the X-Y plane. This plot shows the scatter distribution in water of neutrons emitted from the source in the exposed position, and shows a significant proportion of interactions in the steel shield. The number of interactions are quantified in Table 2.

The simulation shown in Fig. 9(a) and (b) corresponds to the gamma-ray images produced from survey points A and B. These simulated images shows a central hotspot, with other smaller contributions from other areas close to the central location. The plot shown in 9(c) shows the interactions of gamma rays in the environment in the X-Y plane. This plot shows the scatter distribution in water of gamma rays emitted from the source in the exposed position, and shows a significant proportion of interactions in the steel shield. The number of interactions are quantified in Table 3.

5.2. Low Dose Imaging

The ^{252}Cf source was imaged in the stored position to demonstrate the flexibility of the system to conduct long exposure images of low dose sources of radiation. The dose rate at the probe was measured with a portable NMS 17 neutron dosimeter (JCS Ltd, UK) to be below 1 μSv/h, the lower limit of the dosimeter. The probe was moved into close proximity of the steel exterior of the tank, the distance from the detector to the source was 94 cm including 46 cm of water shielding and 3.3 cm of steel shielding. The data collection time t_d at each collimator position was increased by an order of magnitude to 300 s; the duration of the whole image taking 30 days. The monitored neutron and gamma-ray background rates were not seen to drift or change during the imaging routine. The simulated neutron energy spectrum of this configuration was significantly harder when compared with the exposed source imaging, the

Accepted manuscript

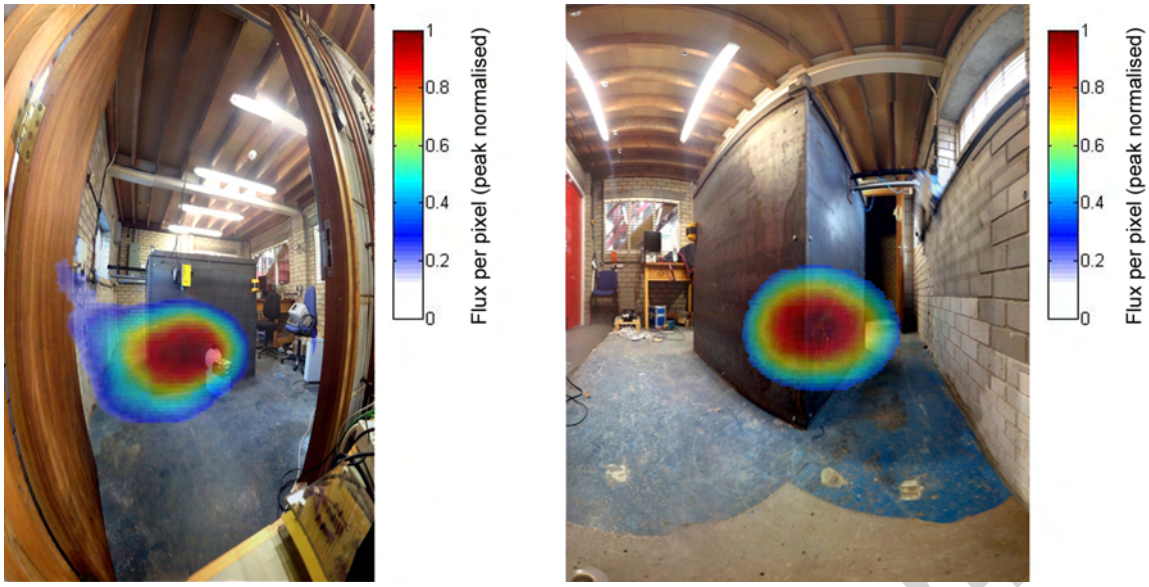

Figure 6: Neutron images of the exposed ^{252}Cf source environment conducted from (a) survey point A and (b) survey point B. Each image clearly identifies the location of the neutron source (^{252}Cf) inside the steel shield containment. These images are also noticeably not radially symmetric from the center-point i.e. it appears that sources of neutrons (other than those emitted directly from the ^{252}Cf source) are contributing to the image solution. Corresponding simulations of these images seen in Fig. 8 suggest that this is primarily due to scattering contributions from the steel shield and a smaller component from the concrete floor and walls.

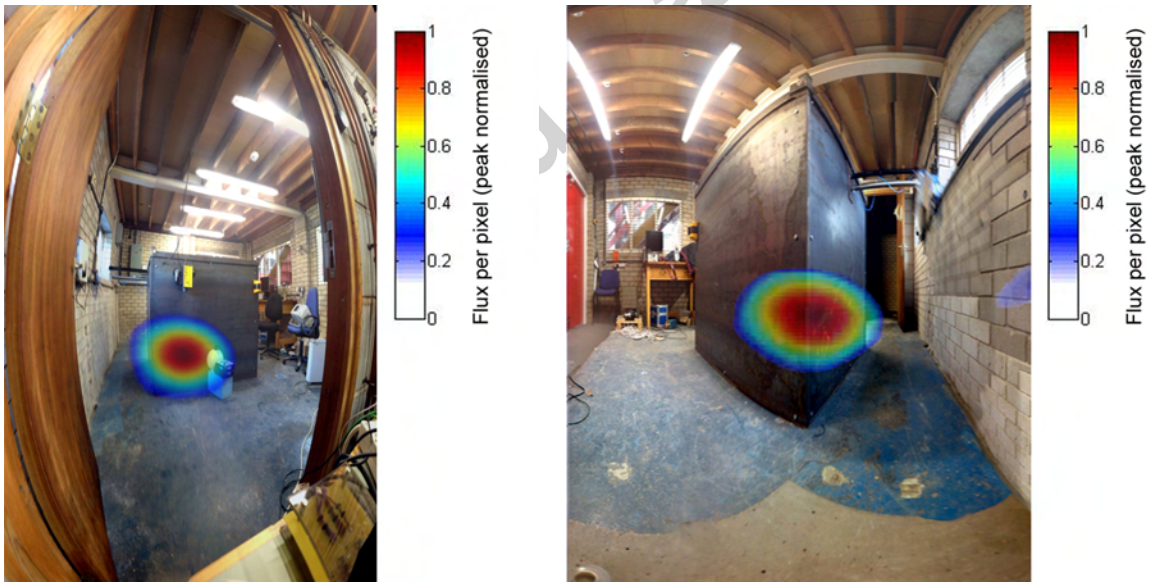

Figure 7: Gamma-ray images of the exposed ^{252}Cf source environment conducted from (a) survey point A and (b) survey point B. Each image clearly identifies the location of the gamma-ray source (^{252}Cf) inside the steel shield containment. These images are also noticeably not radially symmetric from the center-point i.e. it appears that sources of gamma rays (other than those emitted directly from the ^{252}Cf source) are contributing to the image solution. Corresponding simulations of these images seen in Fig. 9 suggest that this is primarily due to scattering contributions from the steel shield and a smaller component from the concrete floor and walls.

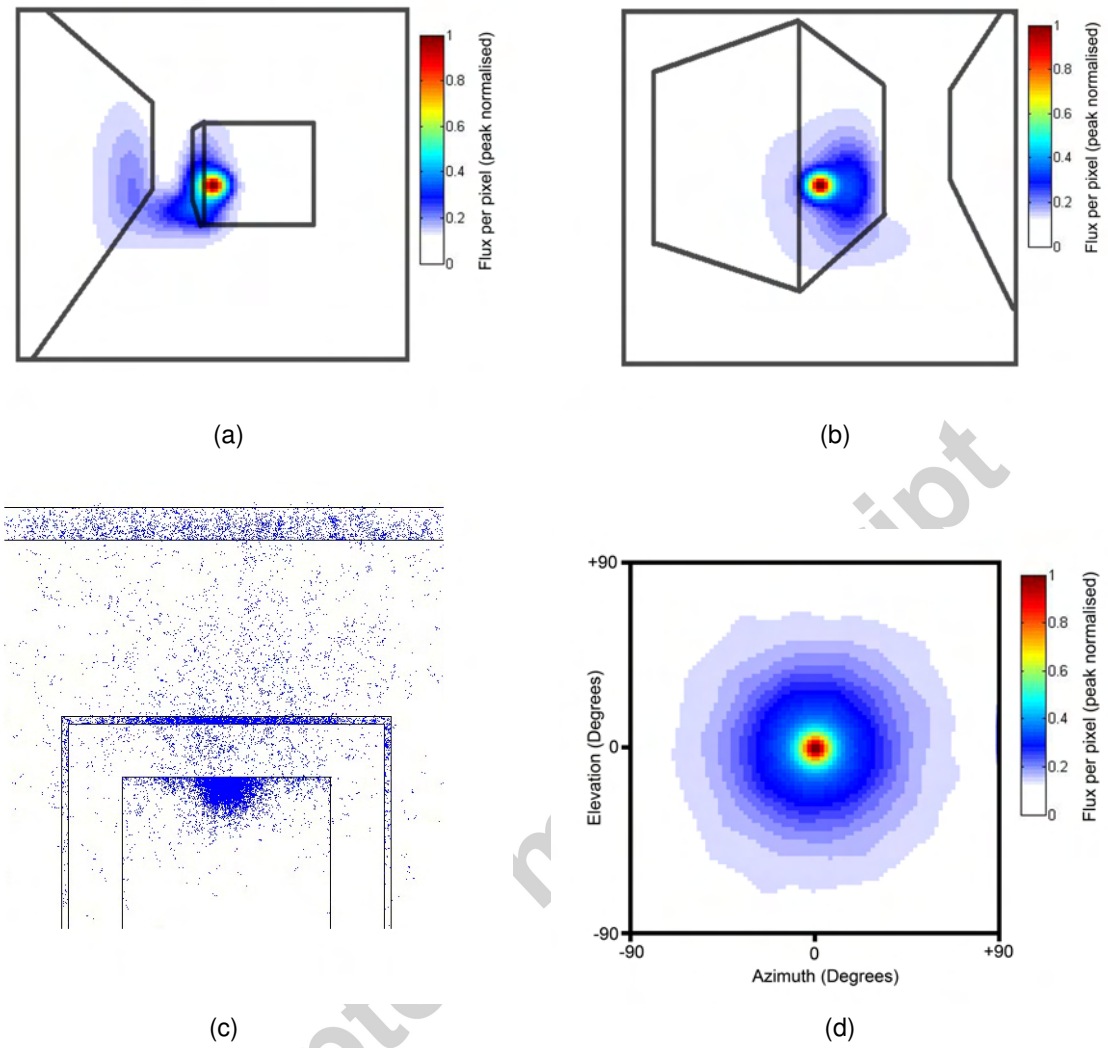

Figure 8: Monte Carlo simulations of the neutron imaging survey. These simulated images (a, b and d) were conducted from corresponding locations of the survey points A, B and C with all relevant features of the environment: radiation source, water tank, steel shielding, concrete floor and walls. The images were created using the pin-hole flux feature in MCNP5 with a perfect pin-hole function. The resulting images were then subjected to a Gaussian blur filter to allow better comparison between these simulated images and the real images. Note that these images are centered upon the location of the ^{252}Cf source and are overlaid on outlines of the steel tank and concrete wall. The colour bar scale indicates the detected neutron flux originating from each 1×1° pixel. The individual images are (a) the simulated image from position A with source exposed (b) the simulated image from position B with source exposed (c) a plot in the X-Y plane of neutron interactions in the water tank and surrounding steel shield with the source in the exposed position (relevant to images a and b) (d) the simulated image from position C with source stored .

simulated neutron flux is given in Fig. 5 though did not effect imaging capabilities. Further information on particle interactions in the simulation are given in Tables 2 and 3

The neutron and gamma-ray image of the this configuration can been seen in Figs. 10(a) and (b) respectively. Each image shows a central radiation hotspot originating from the tank directly in front of the imager. The corresponding simulated neutron and gamma-ray images are shown in Figs 8(d) and 9(d) respectively each depicting a single radially-symmetric hot spot of radiation directly in front of the imager.

6. Discussion and Conclusion

The neutron and gamma-ray images from survey point A are shown in Figs. 6(a) and 7(a) respectively.

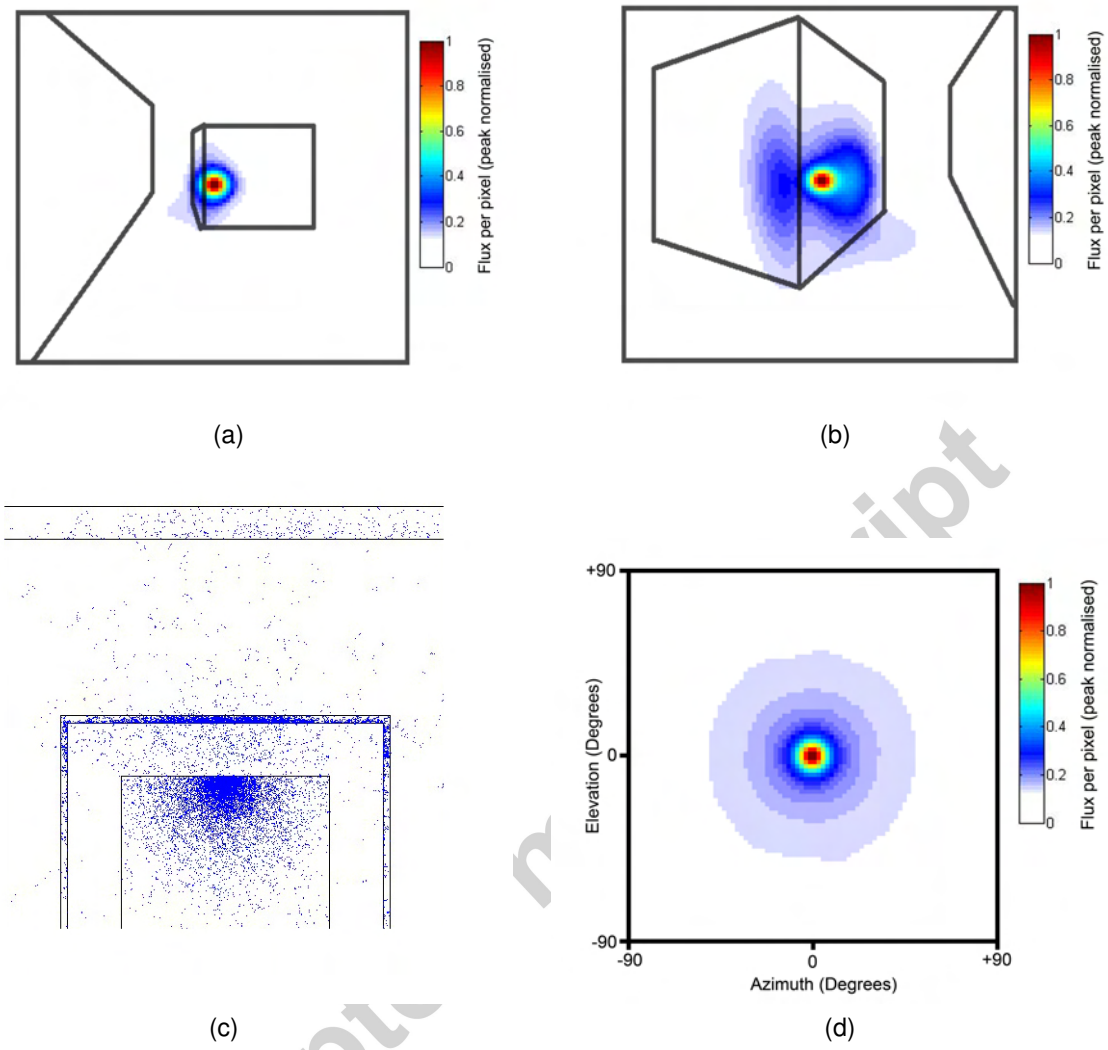

Figure 9: Monte Carlo simulations of the gamma-ray imaging survey. These simulated images (a, b and d) were conducted from corresponding locations of the survey points A, B and C with all relevant features of the environment: radiation source, water tank, steel shielding, concrete floor and walls. The images were created using the pin-hole flux feature in MCNP5 with a perfect pin-hole function. The resulting images were then subjected to a Gaussian blur filter to allow better comparison between these simulated images and the real images. Note that these images are centered upon the location of the ^{252}Cf source and are overlaid on outlines of the steel tank and concrete wall. The colour bar scale indicates the detected gamma-ray flux originating from each 1×1° pixel. The individual images are (a) the simulated image from position A with source exposed (b) the simulated image from position B with source exposed (c) a plot in the X-Y plane of gamma-ray interactions in the water tank and surrounding steel shield with the source in the exposed position (relevant to images a and b) (d) the simulated image from position C with source stored.

The neutron image appears to show a single major hotspot of radiation, plus some contributions and skewing to the left hand side. The gamma-ray image appears to show the source location with a small amount of skewing to the left hand side. This effect is also present in the corresponding simulated pin-hole images for neutrons (Fig. 8(a)) and gamma rays (Fig. 9(a)). This skewing is thought to be associated with scatter from the steel shield in the region closest to the radiation source. The steel is 3.3 cm thick and is shown in MCNP5 simulations to interact significantly with neutrons (Fig. 8(c)) and to a lesser extent with gamma-rays (Fig. 9(c)). The contribution to the skewing in the neutron image is from scatter and production of neutrons in (n, xn) reactions in the steel, though those due to neutron production reactions are calculated to contribute less than 1%. The

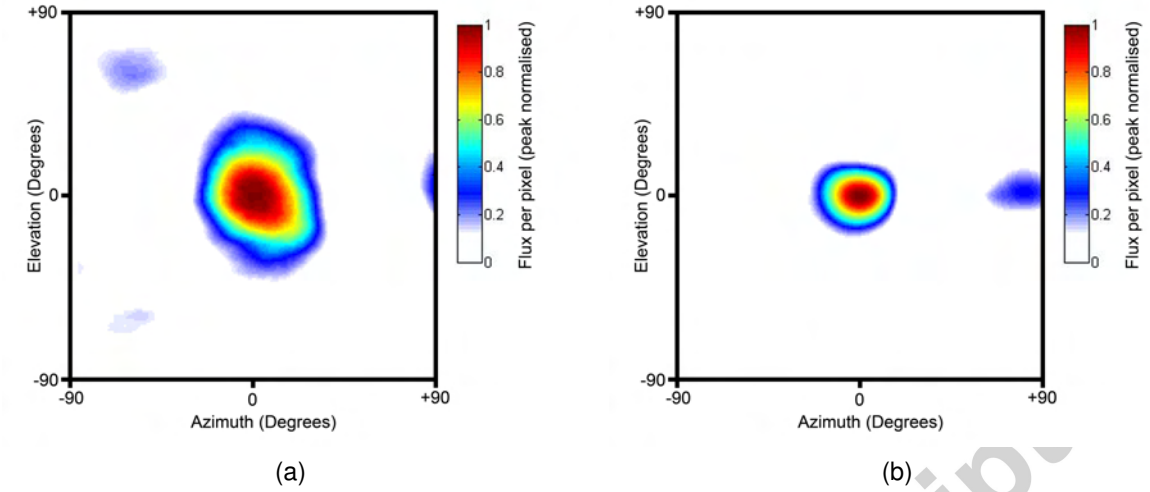

Figure 10: Images taken from survey point C with (a) neutrons and (b) gamma rays. The source was stored in each case and each image correctly identifies the location of the ^{252}Cf source despite 46 cm of water shielding and 3.3 cm of steel between the source and the imaging probe. The neutron and gamma-ray flux escaping the tank in this configuration was very low and comparable to background. This low dose environment was imaged by taking a long-exposure image over 30 days.

Table 2: Further information on neutron particle histories in MCNP simulations indicating the total number of particle histories, the number of tracks escaping the water tank, number of collisions with the steel shield, number of tracks escaping the steel shield, number of secondary neutrons produced in (n,2n) reactions. Only particles above 100 keV neutron energy were counted.

Neutron	Source exposed	Source stored
Histories	1.00×10^{9}	1.00×10^{9}
Escaping water	4.18×10^{8}	3.10×10^{6}
Collisions steel	5.33×10^{8}	1.71×10^{6}
Escaping steel	1.79×10^{8}	1.57×10^{6}
(n,2n) production	1.00×10^{5}	1.67×10^{3}

Table 3: Further information on photon particle histories in MCNP simulations indicating the total number of particle histories, the number of tracks escaping the water tank, number of collisions with the steel shield, number of tracks escaping the steel shield, number of secondary photons produced. Only particles above 10 keV photon energy were counted.

Photon	Source exposed	Source stored
Histories	1.00×10^{9}	1.00×10^{9}
Escaping water	5.69×10^{8}	1.68×10^{8}
Collisions steel	1.25×10^{9}	2.42×10^{8}
Escaping steel	4.69×10^{7}	7.79×10^{6}
Production	7.95×10^{6}	6.20×10^{7}

major consolidated contribution of scatter in this image is calculated from the image simulations to account for 25% of the imaged flux and is located 5° to the left side of the source location. This equates to 21±3 cm in front of the tank agreeing with the location of the steel at 22 cm in front of the source and agrees spatially with the neutron survey image.

The neutron (Fig. 6(b)) and gamma-ray (Fig. 7(b)) images produced at survey point B also show good agreement and similar features; a single hotspot consistent with the position of the ^{252}Cf source. The neutron image does appear to show some skewing to the right hand side, and the gamma-ray image appears flattened. This is consistent with the simulated images in Figs. 8(b) and 9(b).

In these low shielded scenarios the neutron and gamma-ray images determine the location of the hotspot within ±1° in azimuth and elevation of the location of the ^{252}Cf source. It can therefore be concluded that this method is effective at identifying the presence of a single source of neutron and/or gamma-ray radiation and locating in the local environment. The presence of radiation field components other than the major hotspot and their validation from simulations indicate that this imaging method can be used to identify smaller contributions of the radiation fields namely scatter from the

Accepted manuscript

ACCEPTED MANUSCRIPT

steel shield, concrete wall and floor (survey point A neutron image only) in these scenarios.

The neutron and gamma-ray images produced of the stored source shown in Figs. 10(a) and 10(b) respectively each show a single radiation hotspot at the location of the ^{252}Cf source, clearly identifying this source through 46 cm of water shielding and 3.3 cm of steel. The neutron image appears to have some skewing and both images contain artefacts which cannot be attributed to an accurate characterisation of the local radiation fields. These effects were thought to be related to the larger error on the measurements due to the weaker field and the lower signal-to-noise ratio (in relation to the cosmic neutron background and gamma-ray background) when compared with the low-shielded images. These properties also lead to a greater sensitivity to any instabilities in the system which could produce these effects.

The pin-hole simulation image corresponding to the stored source neutron image can be seen in Fig. 8(d) showing a radially symmetric distribution of neutrons with greater dispersion when compared to other pin-hole simulations in Fig. 8. The majority of the imaged neutrons (>99%) have scattered at least once in the water moderator causing this effect. The simulated image for the gamma-ray field shown in Fig. 9(d) shows similar characteristics of a single dispersed hotspot.

The low-dose images of a heavily shielded ^{252}Cf source were validated with Monte Carlo simulations and used to determine the location of the source within $\pm 1^{\circ}$ in azimuth and elevation. It can therefore be concluded that this technique can be used to image low-dose radiation fields ($<1\mu$Sv/h) arising from a spontaneous fission source and determine its location when surrounded by significant amounts of hydrogenous shielding.

Several other systems are able to passively characterise neutron fields through stand-off imaging. The most common is perhaps the neutron scatter camera configuration which has been successfully implemented by several groups in portable forms [22] [23] [24]. Coded aperture systems both in portable [25] and non-portable forms [26] have also been investigated. These imagers have large detection volumes and can therefore rapidly locate sources of fast-neutrons in the local environment making them ideal for nuclear security applications where portability and source location time is critical.

The system discussed in this work uses a single collimated detector with a small detection volume, because of this it has a high compactness and portability and can function in high-dose fields due to the relatively small exposed area of the detector. The collimator also provides some reduction in the contributions from the cosmic neutron background increasing the capability to image weak neutron fields. The deployments best suited for this system are where measurement time is not critical, but where compactness, simplicity and a large operating range with regard to radiation flux are advantageous or where large amounts of hydrogenous material may be present. Such applications may be in nuclear decommissioning or reactor core characterisation for research purposes or for fuel debris location following core damage incidents.

Acknowledgment

The authors wish to acknowledge support (including an EngD studentship to J.S.B.) from the Engineering and Physical Sciences Research Council (Grant Number EP/G037426/1), Createc Ltd. and the Nuclear Decommissioning Authority.

References

[1] J. Beaumont, M. P. Mellor, M. J. Joyce, The analysis of complex mixed-radiation fields using near real-time imaging, Radiat. Prot. Dosimetr. 161 (1-4) (2014) 331–334. arXiv:http://rpd.oxfordjournals.org/content/161/1-4/331.full.pdf+html, doi:10.1093/rpd/ncu044.
URL http://rpd.oxfordjournals.org/content/161/1-4/331.abstract

[2] J. Iwanowska-Hanke, M. Moszynski, L. Swiderski, P. Sibczynski, T. Szczesniak, T. Krakowski, P. Schotanus, Comparative study of large samples (2"× 2") plastic scintillators and ej309 liquid with pulse shape discrimination (psd) capabilities, Journal of Instrumentation 9 (06) (2014) P06014.

[3] M. Joyce, M. Aspinall, F. Cave, A. Lavietes, real-time, digital pulse-shape discrimination in non-hazardous fast liquid scintillation detectors: prospects for safety and security, IEEE Trans. Nuc. Sci 59 (4) (2012) 1245–1251. doi:10.1109/TNS.2011.2174651.

[4] J. Brennan, R. Cooper, M. Gerling, P. Marleau, N. Mascarenhas, S. Mrowka, Applying the neutron scatter camera to treaty verification and warhead monitoring, in: IEEE Nuclear Science Symposuim & Medical Imaging Conference, 2010.

[5] J. K. Polack, A. Poitrasson-Rivière, M. C. Hamel, K. Ide, K. L. McMillan, S. D. Clarke, M. Flaska, S. A. Pozzi, Dual-particle imager for standoff detection of special nuclear material, in: Nuclear Science Symposium and Medical Imaging Conference (NSS/MIC), 2011 IEEE, IEEE, 2011, pp. 1494–1500.

[6] Nuclear Damage Compensation and Decommissioning Facilitation Corporation, Technical strategic plan 2015 for decommissioning of the fukushima daiichi nuclear power station of tokyo electric power company (2015).
URL http://www.dd.ndf.go.jp/ddwp/wp-content/themes/theme1501/pdf/SP2015_20150624_en.pdf

[7] H. Miyadera, K. N. Borozdin, S. J. Greene, Z. Lukic, K. Masuda, E. C. Milner, C. L. Morris, J. O. Perry, Imaging Fukushima Daiichi reactors with muons, AIP Adv. 3 (5). doi:{10.1063/1.4808210}.

Accepted manuscript

ACCEPTED MANUSCRIPT

[8] J. S. Beaumont, M. P. Mellor, M. Villa, M. J. Joyce, High-intensity power-resolved radiation imaging of an operational nuclear reactor, Nat Commun 6 (2015) –.
URL http://dx.doi.org/10.1038/ncomms9592

[9] W. C. Feldman, S. Maurice, A. B. Binder, B. L. Barraclough, R. C. Elphic, D. J. Lawrence, Fluxes of fast and epithermal neutrons from lunar prospector: evidence for water ice at the lunar poles, Science 281 (5382) (1998) 1496–1500.
URL http://www.jstor.org/stable/2895125

[10] D. Herzo, R. Koga, W. Millard, S. Moon, J. Ryan, R. Wilson, A. Zych, R. White, A large double scatter telescope for gamma rays and neutrons, Nucl. Instr. Meth. Phys. Res. A. 123 (3) (1975) 583 – 597. doi:http://dx.doi.org/10.1016/0029-554X(75)90215-3.
URL http://www.sciencedirect.com/science/article/pii/0029554X75902153

[11] N. Mascarenhas, J. Brennan, K. Krenz, P. Marleau, S. Mrowka, Results with the neutron scatter camera, IEEE Trans. Nuc. Sci 56 (3) (2009) 1269–1273, Symposium on Radiation Measurements and Applications, Berkeley, CA, JUN 02-05, 2008. doi:{10.1109/TNS.2009.2016659}.

[12] K. A. A. Gamage, M. J. Joyce, J. C. Adams, Combined digital imaging of mixed-field radioactivity with a single detector, Nucl. Instr. Meth. Phys. Res. A. 635 (1) (2011) 74–77. doi:{10.1016/j.nima.2011.01.033}.

[13] M. P. Mellor, B. Shippen, M. J. Joyce, Efficient single-detector gamma imaging for civil nuclear inspection, in: IEEE Nuclear Science Symp. and Medical Imaging Conf. Rec, 2012, pp. 433–438. doi:10.1109/NSSMIC.2012.6551142.

[14] M. P. Mellor, Radiation imaging apparatus (2014).

[15] Ej-301 scintillator specification sheet (2015).
URL http://www.eljentechnology.com/images/stories/Data_Sheets/Liquid_Scintillators/ej301%20data%20sheet.pdf

[16] M. Joyce, M. Aspinall, F. Cave, A. Lavietes, A 16-channel real-time digital processor for pulse-shape discrimination in multiplicity assay, IEEE Trans. Nuc. Sci 61 (4) (2014) 2222–2227. doi:10.1109/TNS.2014.2322574.

[17] M. J. Joyce (2012).

[18] K. A. A. Gamage, M. J. Joyce, N. P. Hawkes, A comparison of four different digital algorithms for pulse-shape discrimination in fast scintillators, Nucl. Instr. Meth. Phys. Res. A. 642 (1) (2011) 78–83. doi:{10.1016/j.nima.2011.03.065}.

[19] L. Stevanato, D. Cester, G. Nebbia, G. Viesti, Neutron detection in a high gamma-ray background with ej-301 and ej-309 liquid scintillators, Nucl. Instr. Meth. Phys. Res. A. 690 (0) (2012) 96 – 101. doi:http://dx.doi.org/10.1016/j.nima.2012.06.047.
URL http://www.sciencedirect.com/science/article/pii/S0168900212007139

[20] R. Gordon, A tutorial on art (algebraic reconstruction techniques), IEEE Trans. Nuc. Sci 21 (3) (1974) 78–93. doi:10.1109/TNS.1974.6499238.

[21] R. Forster, L. J. Cox, R. F. Barrett, T. E. Booth, J. F. Briesmeister, F. B. Brown, J. S. Bull, G. C. Geisler, J. T. Goorley, R. D. Mosteller, S. E. Post, R. E. Prael, E. C. Selcow, A. Sood, Mcnp¢ version 5, Nuclear Instruments and Methods in Physics Research Section B: Beam Interactions with Materials and Atoms 213 (2004) 82 – 86, 5th Topical Meeting on Industrial Radiation and Radioisotope Measurement Applications. doi:http://dx.doi.org/10.1016/S0168-583X(03)01538-6.
URL http://www.sciencedirect.com/science/article/pii/S0168583X03015386

[22] P. E. Vanier, I. Dioszegi, C. Salwen, L. Forman, Directional stand-off detection of fast neutrons and gammas using angular scattering distributions, in: Nuclear Science Symposium Conference Record (NSS/MIC), 2009 IEEE, IEEE, 2009, pp. 931–935.

[23] A. Poitrasson-Riviere, A.re, M. C. Hamel, J. K. Polack, M. Flaska, S. D. Clarke, S. A. Pozzi, Dual-particle imaging system based on simultaneous detection of photon and neutron collision events, Nuclear Instruments and Methods in Physics Research Section A: Accelerators, Spectrometers, Detectors and Associated Equipment 760 (2014) 40–45.

[24] N. Mascarenhas, J. Brennan, K. Krenz, P. Marleau, S. Mrowka, Results with the neutron scatter camera, Nuclear Science, IEEE Transactions on 56 (3) (2009) 1269–1273.

[25] P. Marleau, J. Brennan, E. Brubaker, M. Gerling, A. Nowack, P. Schuster, J. Steele, Time encoded fast neutron/gamma imager for large standoff snm detection, in: Nuclear Science Symposium and Medical Imaging Conference (NSS/MIC), 2011 IEEE, IEEE, 2011, pp. 591–595.

[26] P. Hausladen, M. A. Blackston, E. Brubaker, D. Chichester, P. Marleau, R. J. Newby, Fast neutron coded-aperture imaging of special nuclear material configurations, Tech. rep., Oak Ridge National Laboratory (ORNL) (2012).

Accepted manuscript